Stable and unstable tiling patterns formed by ABC miktoarm star triblock terpolymers of symmetric interactions

Cody Hawthorne [*], Juntong He, and Qiang Wang [†]

Department of Chemical and Biological Engineering, Colorado State University, 1370 Campus Delivery, Fort Collins, Colorado 80523-1370, USA

Several discrepancies exist among previous self-consistent field calculations of symmetrically interacting ABC miktoarm star triblock terpolymer melts. Here we address this issue by including all known tiling patterns, as well as several lamellar-type phases known to bound the regions in the parameter space occupied by these patterns. After carefully studying the effect of numerical parameters on the free-energy accuracy, the central region of the phase diagram is constructed in detail; both the (3.4.6.4) pattern and the three-dimensional phase of hierarchical-hexagonal lamellae are found to be stable for the first time. The energetic and entropic contributions to the free-energy density of several phases are analyzed and compared in detail to reveal their stability mechanisms, including the important $(3^2.4.3.4)$ pattern. Comparisons to previous studies of the same model system are present throughout, with our results resolving the aforementioned discrepancies and providing a sound basis for future work to build upon.

I. INTRODUCTION

The self- and directed assembly of block copolymers has attracted long-standing interest due to its fundamental and practical importance [1,2]. While the self-assembled morphologies formed by the simplest block copolymer system, linear and flexible diblock copolymer A-B melts with nearly equal statistical segment lengths, are simple and have been well understood [1], adding just one more flexible block C greatly expands the parameter space and leads to many distinct morphologies such that the phase behavior of flexible ABC triblock terpolymer melts remains poorly understood, despite the large amount of efforts devoted to their study; this is the case for both linear and miktoarm (or star) chain architectures [1,3–7].

In this work, we are mainly interested in the various two-dimensional (2D) tiling patterns formed by ABC miktoarm triblock terpolymer melts (referred to as stars hereafter), which are unique due to their underlying chain architecture and tendency to form morphologies rarely found in other block copolymer systems. The tiling patterns, whose structures consist of cylinders with even-sided polygonal cross sections arranged so as to periodically tile the plane, can form when the three arms have comparable block lengths;

such arrangements force the star junctions to align themselves along one-dimensional (1D) lines (either straight or curved) rather than 2D surfaces [8,9]. Each pattern is referred to by a set of integers enclosed in brackets that denote the polygons meeting at a vertex; for example, the well-known honeycomb tiling is referred to as [6.6.6] or [6^3] as three hexagons meet at each vertex. The tiling patterns can be further classified based on whether they correspond to 1 of 11 so-called Archimedean tilings, all of which have the defining characteristic that they contain only one type of vertex. It is possible for tiling patterns to exist that have several types of vertex, however (see Fig. 1), in which case each distinct set of polygons is separated by a semicolon. There are two exceptions to this naming scheme in this paper, [10.6.4;10.8.4] and [8.6.4;8.6^2;12.6.4], which contain several unique vertices while also having a corresponding Archimedean tiling that can be superimposed in a systematic manner. [10.6.4;10.8.4] can be seen to correspond to $(3^2.4.3.4)$ by connecting the centers of the red (A-block) regions in Fig. 1, where we use parentheses rather than brackets to denote that the tiling is superimposed; similarly [8.6.4;8.6^2;12.6.4] can have (3.4.6.4) superimposed by connecting the centers of the blue (B-block) regions in Fig. 1.

While numerous tiling patterns [including those shown in Fig. 1(a)] have been found in experiments [10,11], our focus in this work is on the study of *model*, rather than *real*, melts of ABC stars. Accordingly, we give a brief overview of the previous theoretical and simulation studies of ABC stars having symmetric interactions (i.e., equal repulsion) among segments on different arms, which are also the focus of our study. These studies assume that the three arms have the same statistical segment length and that all polymer segments occupy the same volume, thus providing a well-defined model system that avoids complications in experimental systems.

---

[*]Present address: Department of Chemical Engineering, Pennsylvania State University, University Park, PA 16802, USA.
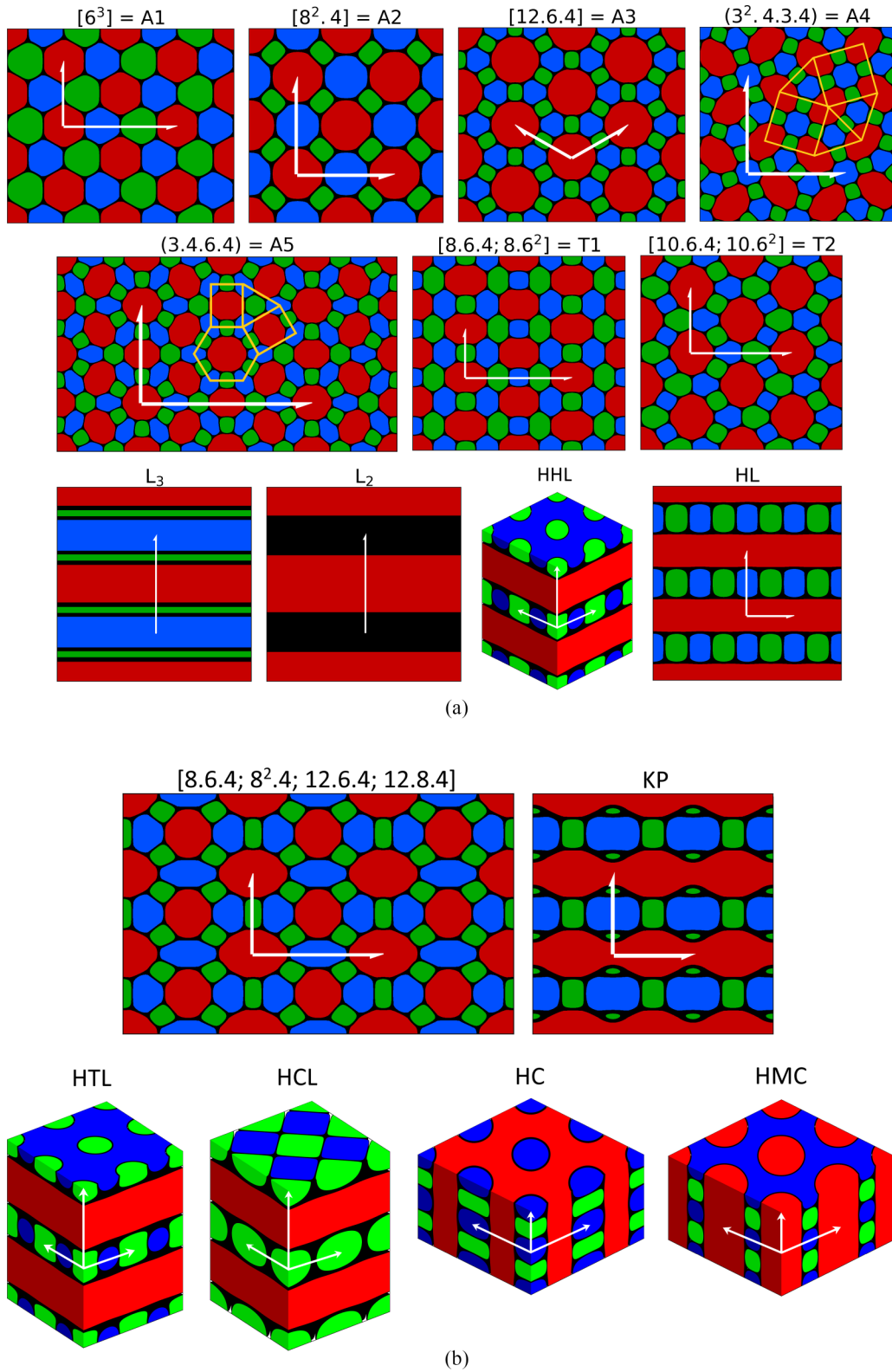
[†]qwang@colostate.edu

FIG. 1. Schematics of some (a) stable and (b) unstable phases formed by symmetrically interacting ABC stars at $\chi N = 30$, constructed from the volume-fraction fields $\{\phi_P(\mathbf{r})\}$ for P = A,B,C. Red, blue, and green correspond to regions where $\phi_P(\mathbf{r}) > 0.5$ for P = A,B,C, respectively, with other regions shown in black. The unit cells used in our SCF calculations are shown by white arrows indicating their basis vectors, and each phase is assigned a simple code name for convenience. See the main text for more details.

TABLE I. Correspondence of various names used for the same self-assembled morphology formed by ABC stars.

Name used in this work	Other names used in the literature
Two-layer lamellae (L_2)	P- and P′-segregated domains within L [23], L_3 [35]
Three-layer lamellae (L_3)	$L_{P,P'}$ with the minority block in the interfaces [23], LAM_3 [27], L3 [31], Lam [34,45], L_3 [35]
Hierarchical lamellae (HL)	L+C [18,22,29,45], $C_P + C_{P'}$ within L [23], LAM+BD [27], LPOC [34], $L_\perp$ [35]
Hierarchical-hexagonal lamellae (HHL)	HPL [34,45]
Hierarchical-tetragonal lamellae (HTL)	QPL [34], TPL [45]
Hierarchical-checkerboard lamellae (HCL)	LAS [34]
Hierarchical gyroid (HG)	$G_\perp$ [35], HDG [45]
Hierarchical cylinders (HCs)	CPD [18], $SWM_{A,B}$ within C_{AB}^{hex} [23], HHC [31,45], $C_\perp$ in the second row of their figure 4(a) [35]
Hierarchical-matrix cylinders (HMCs)	$C_\perp$ in the first row of their figure 4(a) [35]
Core-shell gyroid (CSG)	Gyroid with the minority block in the interfaces [23], Gyroid [34], DG [45]
Core-shell cylinders (CSCs)	CSH [27], HC [31,45], HCyl [34]
Core-shell spheres (CSSs)	Bcc [34,45], S_3 [35]
Perforated lamellae (PL)	Perforated layer [18], $C_A + C_B$ within PL_C [23]

For the simplest case of ABC stars where the three arms have the same length, the $[6^3]$ tiling pattern is expected from symmetry considerations and is indeed found by Dotera and Hatano [12] in their lattice Monte Carlo (LMC) simulations, by Bohbot-Raviv and Wang [13] in their numerical minimization of a free-energy functional obtained under the random-phase approximation for incompressible melts in a 2D unit cell, and by Liang and co-workers in their 2D [14] and 3D [15] calculations of a dynamic density-functional theory [16,17].

Using the aforementioned LMC simulations at the polymer volume fraction $\phi \approx 0.75$ in rectangular cuboid boxes of various sizes, where the three arms of each star are connected to a common joint segment J with the nearest-neighbor interaction parameters $\varepsilon_{PP'} = \varepsilon_{PJ}$ (for P, P′ = A, B, C and P′≠P) and $\varepsilon_{PP} = \varepsilon_{JJ} = 0$, Gemma *et al.* found various morphologies for stars having equal A- and B-arm length (i.e., $N_A = N_B$) with increasing $\gamma \equiv N_C/N_A$, including five tiling patterns ($[8^2.4]$, $[6^3]$, $[8.6.4; 8.6^2]$, $[10.6.4; 10.6^2]$, and $[12.6.4]$), hierarchical lamellae (HL), hierarchical cylinders (HCs), perforated lamellae (PL; i.e., a variant of HL with A and B also penetrating into C layers), A-B lamellae with oblate C spheres at the A-B interfaces, and prolate spheres of A-B lamellae in the C matrix [18]. Table I lists the correspondence of various names used for the same morphology between our work and those in the literature; note that a "hierarchical" morphology is the same as the morphology (e.g., lamellae, gyroid, and cylinders) formed by diblock copolymers but with one domain instead consisting of two microphase-separated domains whose interface is perpendicular to that in the morphology formed by diblock copolymers (if they are parallel, we have a "core-shell" morphology). They also studied $[8^2.4]$, $[6^3]$, $[12.6.4]$, and HL using a strong-stretching theory [18]. In their subsequent simulations in a box of $128 \times 128 \times 10$ (in units of the lattice spacing), Dotera and Gemma [19] found $(3^2.4.3.4)$ for $A_9B_7C_{14}$ (where the subscripts denote the length of each block) and the dodecagonal quasicrystal (DDQC) tiling for $A_9B_7C_{16}$, and Dotera [20] found $[8^2.4]$, DDQC, and $[12.6.4]$

for $A_9B_7C_{12}$, $A_9B_7C_{15}$, and $A_9B_7C_{17}$ and $A_9B_7C_{18}$, respectively. Gemma *et al.* presented a final phase diagram that contains additional morphologies of single diamond and an unknown network, as well as $(3^2.4.3.4)$ found for $A_9B_7C_{14}$ in a simulation box of $48 \times 48 \times 25$ [21]. Very recently, using the same LMC simulations (except with $\varepsilon_{PJ} = 0$) at $\phi \approx 0.9$ with simulated annealing, Li and co-workers found $[8^2.4]$, $[6^3]$, $[8.6.4; 8.6^2]$, and HL for stars having $N_A = N_B = 6$ with increasing $N_C = 2 \sim 15$ [22]. Notably, in the range of $\gamma = 13/6 \sim 15/6$, Gemma *et al.* found $[10.6.4; 10.6^2]$ and/or PL [18] while Li and co-workers found HL [22].

Using dissipative particle dynamics (DPD) simulations at the dimensionless polymer segment number density $\rho\sigma^3 = 3$ in a cubic box of size $(19\sigma)^3$, where σ denotes the range of the nonbonded DPD potential, Huang and co-workers presented two phase diagrams for stars having $N \equiv N_A + N_B + N_C = 20$, where the three arms of each star are connected to a common joint segment J with the dimensionless DPD interaction parameters $a_{PP} = a_{PJ} = 25$ and $a_{PP'} = a$ [23]. In the phase diagram at $a = 36$ (for various star compositions), they found $[8^2.4]$, $[6^3]$, $[10.6.4; 10.6^2]$, $(3^2.4.3.4)$, HL, two-layer lamellae (L_2), three-layer lamellae (L_3), core-shell gyroid (CSG), and tubes (cylinders) formed by mixed two minority blocks (HEX); while in the case of $N_A = N_B$ (for various N_C and a values) they did not find $(3^2.4.3.4)$, but found for the volume fraction of C segments $f_C \equiv N_C/N \leqslant 0.5$ two additional morphologies of micellelike structures with either the two major blocks or all three blocks segregated, and for $f_C \geqslant 0.6$ several additional morphologies including PL, two variants of PL (one referred to as $C_A + C_B$ within PL_{AB} and PL_C, and the other as A- and B-segregated domains within PL_{AB}, in their paper), segmented A- and B-wormlike micelles within either PL_{AB} or a 3D network, AB-formed micelles, and HC [23]. In the case of $N_A = N_B$, their γ values at which $[8^2.4]$, $[6^3]$, and $[10.6.4; 10.6^2]$ are found are consistent with the LMC simulations [18], and that $[8.6.4; 8.6^2]$ is found in the LMC simulations (for $f_C = 0.429 \sim 0.467$) [18,22] but not in the DPD simulations [23] is apparently due to the small N value

used in the latter, where f_C can only be integer multiples of 0.1. Also, the star composition ($f_A = 0.3$ and $f_B = 7/30$) at which ($3^2.4.3.4$) is found in the LMC simulations [18] is close to that ($f_A = 0.3$ and $f_B = 0.2$) in the DPD simulations [23].

Given the differences in the above model systems and that the mismatch between the periodic boundary conditions imposed on the simulation boxes and the bulk periodicity of the self-assembled structures (which is not known in the simulations) can change the structures and their stability [24,25], one can only expect qualitative agreement among the above simulation studies (which is indeed obtained). On the other hand, as we will discuss next, several groups have performed numerical calculations using the polymer self-consistent field (SCF) theory of the "standard" model (i.e., incompressible melts of continuous Gaussian chains with the Dirac δ-function repulsions), where the bulk periodicity of an ordered phase can be readily found by minimizing the Helmholtz free-energy density with respect to the size and shape of the calculation cell. As one may expect, the resulting SCF phase diagram depends on both the ordered phases included in the calculation and the accuracy of their dimensionless Helmholtz free energy per star βf_c (which in turn depends on the spatial and/or chain-contour discretization) used to construct the phase diagram, where $\beta \equiv 1/k_B T$ with k_B denoting the Boltzmann constant and T the thermodynamic temperature of the system.

Tang *et al.* performed 2D SCF calculations with a combinatorial screening strategy [26], where they solved the modified diffusion equations (MDEs) using a Crank-Nicholson scheme and the alternating direction implicit (CN-ADI) method with chain-contour discretization of $\Delta s = 0.01$ and spatial discretization of $\Delta x = \Delta y = (\sqrt{6}/10)R_g$, where R_g denotes the root-mean-square radius of gyration of an *ideal* and *linear* chain having N segments [27]. They constructed a phase diagram for stars at $\chi_{PP'}N = 35$, where $\chi_{PP'}$ denotes the Flory-Huggins parameter characterizing the repulsion between two segments of different types, as a function of f_A and f_B taken to be integer multiples of 0.1, which includes [6^3], [$8^2.4$], L$_3$, HL, HEX, core-shell cylinders (CSCs), and the knitting pattern (KP) [27]. Qiu and co-workers also performed 2D SCF calculations, where they solved the MDEs using the generic reciprocal-space method [28] (which has no chain-contour discretization) with 151 basis functions (corresponding to spatial discretization of $\Delta x = D_x/18$ and $\Delta y = D_y/10$ with D_x and D_y denoting the bulk period of a self-assembled structure along the x and y direction, respectively, which is comparable to that used in Ref. [27]) [29]. They constructed a phase diagram for stars at $\chi_{PP'}N = 30$, which includes [6^3], [$8^2.4$], [12.6.4], [8.6.4; 8.6^2], [10.6.4; 10.6^2], [8.6.4; $8^2.4$; 12.6.4; 12.8.4], L$_3$, and HL; while they used a much smaller increment of 0.001 in f_P, they focused only on the central portion (i.e., $f_P > 0.2$ for any P) of the phase diagram [29]. Apart from the different phases included in these calculations, the reciprocal-space method is expected to give more accurate results than the CN-ADI method.

Li and co-workers solved the MDEs using the second-order pseudospectral method [30] with $\Delta s = 0.001$ and a spatial discretization grid of 128^2 or 64^3 for a calculation cell containing one or two unit cells of an ordered phase (such that the grid spacing is less than $0.1R_g$), and constructed a

phase diagram for stars at $\chi_{PP'}N = 60$, which includes [6^3], [$8^2.4$], [12.6.4], [8.6.4; 8.6^2], [10.6.4; 10.6^2], ($3^2.4.3.4$), L$_3$, HL, CSCs, and HCs; they also included (3.4.6.4) in their calculations but found it to be unstable [31]. The central portion of the phase diagram that Li and co-workers focused on is somewhat larger than in Ref. [29], and apart from the different phases included, their results are in good agreement in most cases. Note that the spatial discretization used in Ref. [31] is finer than in Ref. [29]. In the case of $f_B = f_C$, [12.6.4] is stable for $0.513 \leqslant f_A \leqslant 0.566$ in Ref. [31] but unstable in Ref. [29]; the stable regions of [6^3], [$8^2.4$], and [10.6.4; 10.6^2] found in Ref. [31] are also larger than those in Ref. [29] (with the opposite occurring for [8.6.4; 8.6^2]). These could be due to their different values of $\chi_{PP'}N$.

Zhang and co-workers solved the MDEs using a fourth-order pseudospectral method [32,33] with $\Delta s \leqslant 0.01$ and a spatial discretization grid of 32^3 for a unit cell, and constructed a phase diagram consisting of five lines connecting the central point at $f_A = f_B = 1/3$ to those at $f_C = 0$ and $f_B = 0, 0.17, 0.22, 0.33$, and 0.5, respectively, for stars at $\chi_{PP'}N = 30$, which includes [6^3], [$8^2.4$], [8.6.4; 8.6^2], ($3^2.4.3.4$), L$_3$, HL, CSCs, core-shell spheres (CSSs), CSG, HEX, gyroid formed by mixed B and C, and hierarchical-tetragonal lamellae (HTL) [34]. They actually included many more ordered structures in their calculations and found, in particular, [12.6.4], [10.6.4; 10.6^2], (3.4.6.4), and [8.6.4; $8^2.4$; 12.6.4; 12.8.4] to be unstable along the five lines [34]. Their spatial discretization, however, may not be enough to give accurate results; in the case of two blocks having the same length, for example, Refs. [29,34] give quantitatively different phase boundaries even for the same phases included in both studies.

Finally, Qian and Xu solved the MDEs using the second-order pseudospectral method [30] (with the chain-contour and spatial discretization not given but presumably the same as in Ref. [31]), and constructed a phase diagram for stars at $\chi_{PP'}N = 60$ in the case of $f_B = f_C$, which includes [6^3], [$8^2.4$], L$_2$, L$_3$, HL, HCs, hierarchical-matrix cylinders (HMCs), hierarchical gyroid (HG), and CSSs [35]. The authors noted that the stable region of HMCs they found for $0.46 < f_A < 0.48$ may actually be occupied by some tiling pattern not included in their calculations [35].

The discrepancies between these previous SCF results raise the following question: What are the stable and unstable phases formed by this simple model system? Here we address this question by performing SCF calculations of the "standard" model for symmetrically interacting ABC stars at $\chi_{PP'}N \equiv \chi N = 30$, focusing on the central portion (i.e., $f_P \gtrsim 0.2$ for any P) of the phase diagram as this is the region mostly occupied by the tiling patterns. By including all of the presently discovered tiling patterns from theories and experiments (overlapping many of the candidate pools of previous SCF studies) and accurately computing their free-energy density, we definitively establish which of these patterns are stable at the selected degree of segregation. Additionally, we investigate the energetic and entropic contributions to the free-energy density of the patterns in order to understand what drives their stability, focusing particularly on the differences between the lamellar-type phases [i.e., L$_2$, L$_3$, HL,

hierarchical-hexagonal lamellae (HHL), and HTL] and tiling patterns, as well as the thermodynamic and morphological properties of stable complex tiling patterns [i.e., $(3^2.4.3.4)$ and $(3.4.6.4)$].

II. MODEL AND METHOD

A. SCF equations for the "standard" model

As in Refs. [27,29,31,34,35], here we consider the "standard" model (i.e., an incompressible melt of continuous Gaussian chains interacting via the Dirac δ-function potential) for n miktoarm star triblock terpolymer chains in volume V at thermodynamic temperature T. Each terpolymer chain (referred to as a star) consists of three linear blocks, denoted by $P(=A, B, C)$, connected at a common junction with each P block having N_P segments. For simplicity, we assume that all segments have the same volume $\rho_0^{-1} \equiv V/nN$ with $N \equiv \sum_P N_P$; the average volume fraction of P, equivalent to the block fraction, is therefore given by $f_P \equiv N_P/N$.

In the "standard" model, the configuration of the P block in the kth star is given by a continuous curve $\mathbf{R}_{k,P}(s)$ in space, where $s \in [0, f_P]$ is the block-contour variable with $s = 0$ corresponding to the free end and f_P to the star junction. The dimensionless bonded energy of the P block is then given by $\beta u_{k,P}^b = \int_0^{f_P} ds (d\mathbf{R}_{k,P}(s)/ds)^2/4R_g^2$, where $\beta \equiv 1/k_B T$ with k_B denoting the Boltzmann constant, and $R_g \equiv \sqrt{N/6}a$ with a being the effective bond length assumed to be the same for all the blocks; note that $N \to \infty$ and $a \to 0$ while R_g is finite. On the other hand, the dimensionless nonbonded interaction energy (for stars of symmetric interactions) is given by $\beta U^{nb} = (\chi \rho_0/2) \int d\mathbf{r} \sum_P \sum_{P' \neq P} \hat{\phi}_P(\mathbf{r}) \hat{\phi}_{P'}(\mathbf{r})$, where χ denotes the Flory-Huggins parameter characterizing the repulsion between two segments of different types and $\hat{\phi}_P(\mathbf{r}) \equiv (N/\rho_0) \sum_{k=1}^n \int_0^{f_P} ds \, \delta(\mathbf{r} - \mathbf{R}_{k,P}(s))$ denotes the normalized microscopic number density of P segments at spatial position $\mathbf{r}$. The canonical partition function of this model system can therefore be written as

$$Z = \frac{1}{n!} \int \prod_{k=1}^n \prod_P D\mathbf{R}_{k,P} \cdot \exp\left(-\sum_{k=1}^n \sum_P \beta u_{k,P}^b - \beta U^{nb}\right)$$
$$\times \prod_{\mathbf{r}} \delta\left(\sum_P \hat{\phi}_P(\mathbf{r}) - 1\right)$$
$$\times \prod_{k=1}^n \delta(\mathbf{R}_{k,A}(f_A) - \mathbf{R}_{k,B}(f_B))\delta(\mathbf{R}_{k,B}(f_B) - \mathbf{R}_{k,C}(f_C)),$$

where the first Dirac δ-function enforces the incompressibility constraint at $\mathbf{r}$ while the others enforce the star chain architecture.

The SCF equations for the above model are given by

$$\omega_P(\mathbf{r}) = \chi N \sum_{P' \neq P} \phi_{P'}(\mathbf{r}) + \eta(\mathbf{r}), \tag{1}$$

$$\phi_P(\mathbf{r}) = \frac{1}{Q} \int_0^{f_P} ds \, q_P(\mathbf{r}, s) q_P^\dagger(\mathbf{r}, s), \tag{2}$$

$$\sum_P \phi_P(\mathbf{r}) = 1, \tag{3}$$

where $\phi_P(\mathbf{r})$ is the normalized number density (i.e., volume fraction) field of P segments constrained to $\hat{\phi}_P(\mathbf{r})$, $\omega_P(\mathbf{r})$ is the conjugate field imposing this constraint, and $\eta(\mathbf{r})$ is the conjugate field imposing the incompressibility constraint at $\mathbf{r}$. $q_P(\mathbf{r}, s)$ and $q_P^\dagger(\mathbf{r}, s)$ are the forward and backward one-end-integrated propagators for the P block, satisfying the MDEs

$$\frac{\partial q_P}{\partial s} = \nabla^2 q_P - \omega_P(\mathbf{r}) q_P \tag{4}$$

with the initial condition of $q_P(\mathbf{r}, s = 0) = 1$ and

$$-\frac{\partial q_P^\dagger}{\partial s} = \nabla^2 q_P^\dagger - \omega_P(\mathbf{r}) q_P^\dagger \tag{5}$$

with the initial condition of $q_P^\dagger(\mathbf{r}, s = f_P) = \prod_{P' \neq P} q_{P'}(\mathbf{r}, f_{P'})$, respectively.

$$Q = \frac{1}{V} \int d\mathbf{r} \, q_P(\mathbf{r}, s) q_P^\dagger(\mathbf{r}, s) \tag{6}$$

is the normalized single-star partition function; note that Q is independent of P and s, and we have taken R_g as the unit of length in Eqs. (1)~(6). After these equations are solved, the dimensionless mean-field Helmholtz free energy per star can be calculated (within a constant) as

$$\beta f_c = \frac{\chi N}{2V} \int d\mathbf{r} \sum_P \sum_{P' \neq P} \phi_P(\mathbf{r}) \phi_{P'}(\mathbf{r})$$
$$- \frac{1}{V} \int d\mathbf{r} \sum_P \omega_P(\mathbf{r}) \phi_P(\mathbf{r}) - \ln Q, \tag{7}$$

which must be minimized with respect to (up to six) unit-cell parameters $\boldsymbol{\theta}$ for each ordered phase to find its bulk periodicity; for the "standard" model, this gives [36]

$$\frac{\partial Q}{\partial \boldsymbol{\theta}} = \mathbf{0}. \tag{8}$$

B. Numerical methods and calculated quantities

For a given set of model parameters f_P and χN, discretization parameters $n_\mathbf{r}$ and n_s (explained in Sec. IIIA below), and initial guess $\mathbf{x}^{(0)} \equiv \{\boldsymbol{\theta}^{(0)}, \{\omega_P^{(0)}(\mathbf{r})\}\}$ for an ordered phase, we solve the above SCF equations using the recently released C++/CUDA version [37] of PSCF [38], an open-source code for SCF calculations of the "standard" model for block copolymer self-assembly that takes advantage of the massive parallelization provided by graphics processing units [39]. PSCF uses a fourth-order pseudospectral method [40] to solve Eqs. (4) and (5), the composite Simpson's (1/3) rule to evaluate the chain-contour integral in Eq. (2), the composite trapezoidal rule to evaluate the integral over $\mathbf{r}$ in Eq. (6), and the Anderson mixing [41] combined with a variable-cell scheme [42] to simultaneously solve Eqs. (1), (3), and (8), which can be rewritten as $\mathbf{f}(\mathbf{x}) = \mathbf{0}$ with the convergence criterion of $|\mathbf{f}|_{max} < \varepsilon$ (our choice of ε is also given in Sec. IIIA below). As our improvement of PSCF, we have implemented the option to control the order of the Richardson extrapolation K that is used in solving the MDEs and evaluating the chain-contour integral in Eq. (2) [43] (see the Appendix for more information); our improved code is freely available at https://github.com/qwcsu/PSCFplus.

After solving the above SCF equations, we further calculate the dimensionless mean-field internal energy per star $\beta u_c = \sum_P \sum_{P' \neq P} \beta u_{c,PP'}/2$ with $\beta u_{c,PP'} = \chi N \int d\mathbf{r}\, \phi_P(\mathbf{r}) \phi_{P'}(\mathbf{r})/V$ being the contribution due to the P-P′ repulsion, and the dimensionless entropy per star $s_c/k_B = \sum_P s_{c,P}/k_B + s_{c,J}/k_B$ with $s_{c,P}/k_B \equiv \int d\mathbf{r}\,[\omega_P(\mathbf{r})\phi_P(\mathbf{r}) + \rho_J(\mathbf{r})\ln q_P(\mathbf{r}, f_P)]/V$ due to the conformational entropy of the P block and $s_{c,J}/k_B \equiv -\int d\mathbf{r}\,\rho_J(\mathbf{r})\ln \rho_J(\mathbf{r})/V$ due to the translational entropy of the junction, where $\rho_J(\mathbf{r}) \equiv \prod_P q_P(\mathbf{r}, f_P)/Q$ is the normalized number density of junctions satisfying $\int d\mathbf{r}\, \rho_J(\mathbf{r}) = V$ [44]; clearly, $\beta f_c = \beta u_c - s_c/k_B$.

III. RESULTS AND DISCUSSION

The phases known to play a significant role in symmetrically interacting ABC stars are well established [29,31,34], and here we primarily seek to determine which tiling patterns are stable using the polymer SCF calculations of the "standard" model. Consequently, we consider as candidate phases all regular tiling patterns known from past studies, both theoretical and experimental, as well as several lamellar-type phases (in order to compute their phase boundaries with the tiling patterns). These include all the phases shown in Fig. 1; note that we were able to obtain converged results of KP and HCL only at a few points in the f_P parameter space. Though our list is not exhaustive, it includes many phases known from previous work to form near the central region of the phase diagram and importantly overlaps with the candidate pools of previous studies, thus resolving the discrepancies that may have arisen from using different candidates in previous SCF calculations.

In the remainder of this section, we first describe the impact of numerical parameters and justify that our choices give sufficient numerical accuracy in Sec. IIIA. This is followed in Sec. IIIB by a presentation of the phase diagram at the segregation strength $\chi N = 30$, as well as the dimensionless Helmholtz free energy per star βf_c and its components along the $f_B = f_C$ isopleth. Section IIIC finishes with an investigation of the thermodynamic properties of stable complex tiling patterns $(3^2.4.3.4)$ and $(3.4.6.4)$, uncovering the effects that stabilize them and comparing these amongst various morphologies; the star junction density $\rho_J(\mathbf{r})$ of various tiling patterns is also presented.

A. Numerical accuracy

For a given set of system parameters f_P and χN, there are four numerical parameters that control the accuracy of our SCF calculations of an ordered phase: the maximum absolute value of the residual errors of the converged SCF equations (i.e., the convergence criterion) ε, the total number of spatial discretization points $n_{\mathbf{r}}$, the total number of chain-contour discretization intervals $n_s = \sum_P n_P$, and the order of the Richardson extrapolation K that is used to solve the modified diffusion equations. Outside of the error analysis in this section, we set $\varepsilon = 10^{-5}$ and allow PSCF [37] to adjust the unit-cell parameters in order to minimize βf_c for all of our results presented. For the error analysis, the unit-cell parameters are held constant (very close to those minimizing βf_c) so as to examine solely the effect of the
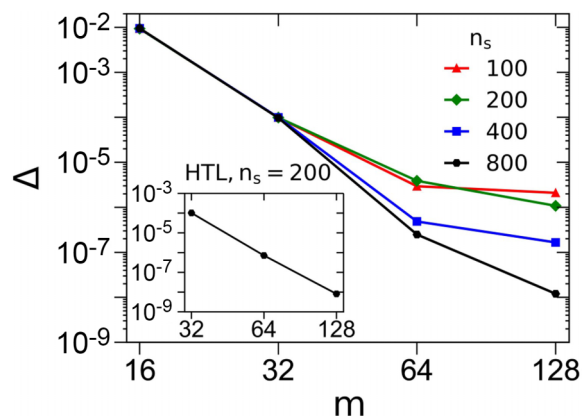

FIG. 2. Logarithmic plot of the error $\Delta \equiv |\beta f_c(m, n_s, K = 1) - \beta f_c^*|$ in the SCF Helmholtz free energy per star βf_c as a function of the spatial discretization parameter m and the chain-contour discretization parameter n_s for $(3^2.4.3.4)$ and HTL (inset). Results for $(3^2.4.3.4)$ are shown at the ABC star composition $(f_A = 0.45, f_B = 0.30)$ and for HTL at $(f_A = 0.50, f_B = 0.30)$, both at $\chi N = 30$. A square mesh of $n_{\mathbf{r}} = m^2$ and cubic mesh of $n_{\mathbf{r}} = m^3$ is used for $(3^2.4.3.4)$ and HTL, respectively, with $\beta f_c^* = \beta f_c(m = 256, n_s = 1600, K = 4)$ for $(3^2.4.3.4)$ and $\beta f_c^* = \beta f_c(m = 128, n_s = 800, K = 3)$ for HTL; the convergence criterion of $\varepsilon = 10^{-9}$ for solving the SCF equations is used in both cases. In units of R_g, the unit-cell parameters are 8.41 for $(3^2.4.3.4)$ and $(3.48, 3.98)$ for HTL. See the main text for more details.

numerical parameters on the accuracy of βf_c of an ordered phase. In practice, we find the differences in βf_c between different phases to always be greater than our choice of $\varepsilon = 10^{-5}$, allowing the stable phase (of those considered) at each point in the system parameter space to be resolved unambiguously, provided that $n_{\mathbf{r}}$ and n_s are large enough to also give an accuracy of $\beta f_c(n_{\mathbf{r}}, n_s, K)$ higher than 10^{-5}. Note that the parameter K affects both the accuracy of βf_c and the accessible points in the f_P parameter space and should thus be chosen judiciously. As discussed in the Appendix, the block-contour discretization n_P is constrained to integer multiples of 2^K; since the block fraction $f_P = n_P/n_s$, this also constrains the values that f_P can take for given n_s. With this in mind, $K = 1$ (i.e., the fourth-order pseudospectral method [40] implemented in PSCF) is used to obtain all subsequent results while higher-order (i.e., $K > 1$) methods are used only to obtain highly accurate values of βf_c, denoted by $\beta f_c^* \equiv \beta f_c(n_{\mathbf{r}}^{\max}, n_s^{\max}, K^{\max})$, for use in the error analysis. The error in $\beta f_c = \beta f_c(n_{\mathbf{r}}, n_s, 1)$ of an ordered phase is then measured by $\Delta(n_{\mathbf{r}}, n_s) \equiv |\beta f_c(n_{\mathbf{r}}, n_s, 1) - \beta f_c^*|$. This error must be analyzed for each ordered phase, particularly with respect to its variation with $n_{\mathbf{r}}$ and n_s as the values necessary to achieve a desired accuracy depends on the complexity of the phase, the size of its unit cell, and the segregation strength χN (which is set to 30 in this work).

For example, Fig. 2 and its inset show $\Delta(n_{\mathbf{r}}, n_s)$ for $(3^2.4.3.4)$ and HTL, respectively, serving as representative results for 2D and 3D phases. Rather than $n_{\mathbf{r}}$, the horizontal axis m denotes the number of spatial discretization intervals along each direction of the unit cell; note that a square unit cell is used for $(3^2.4.3.4)$ and a tetragonal unit cell for HTL. We
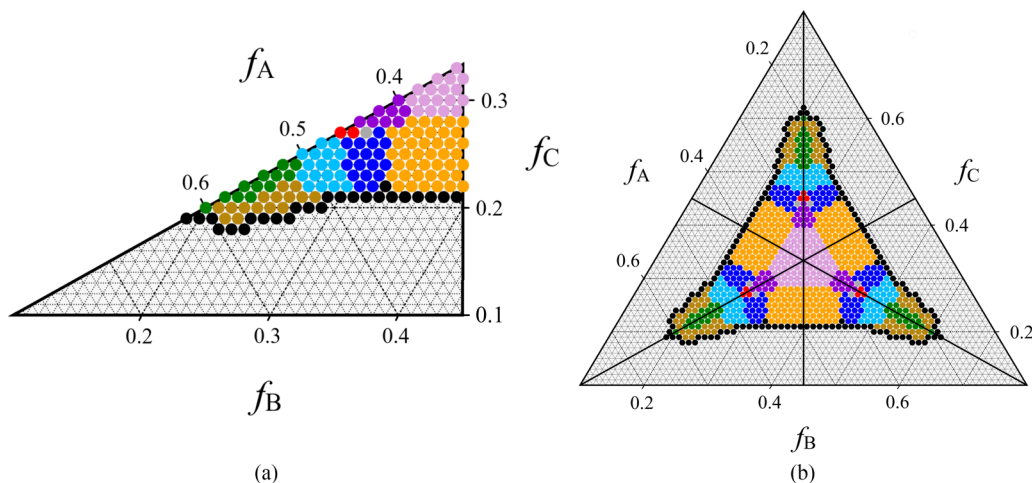
FIG. 3. Central region of our SCF phase diagram of ABC stars of symmetric interactions at $\chi N = 30$. Each dot shows the stable phase at that point, color-coded according to [6³]: pink; [8².4]: orange; [12.6.4]: cyan; (3².4.3.4): blue; (3.4.6.4): gray; [8.6.4; 8.6²]: purple; [10.6.4; 10.6²]: red; L: black; HL: green; and HHL: brown. Symmetric interactions reduce the necessary area to 1/6 of the parameter space as shown in part (a), which is used to reconstruct the full phase diagram in (b). $K = 1$ and $n_s = 200$ are used in our SCF calculations. See the main text for more details.

see in Fig. 2 that for small m, Δ curves for various n_s overlap as the errors are dominated by the spatial discretization, while for large m, Δ curves begin to level off as the errors are now dominated by the chain-contour discretization. From these results, it is clear that $n_s = 200$ is sufficient to yield $\Delta < 10^{-5}$ for both (3².4.3.4) and HTL by taking $m = 128$ for the former and $m = 64$ for the latter. In fact, this n_s value is sufficient to give $\Delta < 10^{-5}$ for all phases considered in this work and has the additional benefit that with $K = 1$ all accessible f_P values are integer multiples of 0.01, providing a high-resolution discretization of the parameter space. For this reason, $n_s = 200$ is used in our subsequent SCF calculations. The effect of $n_{\mathbf{r}}$ on Δ for all other phases is also studied in a similar manner, and we find that $n_{\mathbf{r}} = 128 \times 256$, 128^2, 128^2, 128×256, 128×288, 160×240, 128×256, 128, 160×192, 128^2, and 64^3 for [6³], [8².4], [12.6.4], (3.4.6.4), [8.6.4; 8.6²], [10.6.4; 10.6²], [8.6.4; 8².4; 12.6.4; 12.8.4], lamellae (L, including both L_2 and L_3), HL, KP, and all 3D phases, respectively, ensure $\Delta < 10^{-5}$ in all cases; these are used to construct the phase diagram in Sec. IIIB.

B. Phase diagram and free-energy data

To construct the phase diagram at $\chi N = 30$, at each accessible point in the central region of the f_P parameter space we compute βf_c for all competing phases and take the phase having the smallest βf_c as the stable one at that point. The results are shown in Fig. 3, where the different stable phases are shown in different colors. The symmetry-reduced phase triangle (where calculations are carried out) is given in Fig. 3(a), where $f_A > f_B > f_C$ at all points except for the $f_B = f_C$ isopleth that forms the hypotenuse and the $f_A = f_B$ isopleth that bounds the triangle to the right. Note that the central region of the parameter space where tiling patterns are stable is enclosed by L in our SCF calculations.

Figure 3 shows that there are a total of seven stable tiling patterns at $\chi N = 30$, including [12.6.4], (3².4.3.4),

(3.4.6.4), [8.6.4; 8.6²], and [10.6.4; 10.6²] in addition to the well-established [6³] and [8².4]. The tiling patterns transition to L as one progresses radially outward in the phase diagram. We note that L occurs in two variations: L_3, where there exist three microphase-separated layers each mainly consisting of one species, and L_2, where the two minority (B and C) blocks mix to form a layer between those of the majority (A) block. Though no distinction is made between these two morphologies in Fig. 3, we have found that L_2 forms when both f_B and f_C are small and comparable to each other, while L_3 forms when they are significantly different; for example, in Fig. 3(a) L_2 occurs near the $f_B = f_C$ isopleth while L_3 occurs near the $f_A = f_B$ isopleth. As the minority blocks become smaller and their size disparity decreases, trial (i.e., initial) fields for L_3 converge instead to L_2 in our SCF calculations, the stability of which is probably due to either the relatively weak segregation of $\chi N = 30$ considered here or the limited pool of candidate phases (which does not include, e.g., the perforated lamellae found in molecular simulations [18,23]). SCF calculations at a stronger segregation of $\chi N = 60$ by Li *et al.* [31] suggest that the stability of L shrinks dramatically as χN increases, most likely from the destabilization of L_2 relative to other morphologies.

The most novel of these results are the regions of stability of (3.4.6.4) and HHL. These phases are found stable in ABC stars of symmetric interactions for the first time, although both have been considered in previous SCF studies [31,34] of these systems and HHL was found stable for stars of asymmetric interactions [45]. With the parameter-space discretization used here, (3.4.6.4) is stable at a single point ($f_A = 0.44$, $f_B = 0.29$) with its βf_c on the order of 10^{-3} smaller than the competing tiling patterns [i.e., (3².4.3.4), [10.6.4; 10.6²], and [8.6.4; 8.6²]]. To the best of our knowledge, HHL was considered in only one SCF study of symmetrically interacting ABC stars [34] where HTL was reported as stable instead. In contrast to that study, we find that HHL is always more stable than HTL in the region considered here, with βf_c of HHL on

the order of 10^{-3} smaller than HTL in most cases. According to our SCF calculations, HHL is the only stable 3D phase that appears in this region as HC, HMC, and HCL have either prohibitively large βf_c or simply could not be converged on at any of the points considered. Notably, HMC is not stable in the region of $0.46 < f_C < 0.48$ as found in Ref. [35], since $[10.6.4; 10.6^2]$ holds a small region of stability here. It is possible, however, that HC, HMC, or HCL could appear outside of the region of parameter space considered here. HC, for example, is most likely stable along the $f_B = f_C$ isopleth for larger values of f_A as we observe a downward trend in its βf_c along this line (data not shown); it is less likely that HMC or HCL is stable at any point for a symmetrically interacting system owing to the observed trend in their βf_c as well as the difficulty in obtaining converged results for these phases.

As discussed in the Introduction, there exist several previous SCF studies of this system that contain conflicting results, even for the same candidate phases considered. In particular, Ref. [34] found $[12.6.4]$, $[10.6.4; 10.6^2]$, $[8.6.4; 8^2.4; 12.6.4; 12.8.4]$, $(3.4.6.4)$, and HHL to be unstable at $\chi N = 30$ along the five lines connecting the center of the f_P parameter space to an edge of the phase triangle, while Ref. [29] found the former three tiling patterns to be stable at $\chi N = 30$ and Ref. [31] found the former two (but not $[8.6.4; 8^2.4; 12.6.4; 12.8.4]$) to be stable at $\chi N = 60$. On the other hand, Refs. [31,34] found $(3^2.4.3.4)$ to be stable with its region of stability much larger at $\chi N = 30$ in Ref. [34] than at $\chi N = 60$ in Ref. [31], while this phase was not considered in Ref. [29]. In addition to these differences in phase stability, Refs. [29,34] (both at $\chi N = 30$) also gave quantitatively different phase boundaries for the same phases; taking the $f_A = f_B$ isopleth as an example, Ref. [29] found the $[8^2.4]/[6^3]$ and $[6^3]/[8.6.4; 8.6^2]$ transitions to occur at $f_C = 0.28$ and $f_C = 0.39$, respectively, while Ref. [34] found these same phase transitions at $f_C = 0.265$ and $f_C = 0.41$, respectively. Clearly, such discrepancies raise questions concerning the accuracy and reproducibility of these previous SCF results, which we have addressed with the error analysis in Fig. 2 and thorough SCF calculations in Fig. 3. Our results definitively show that $[12.6.4]$, $[10.6.4; 10.6^2]$, and $(3.4.6.4)$ are stable tiling patterns at $\chi N = 30$ and confirm the stability of $(3^2.4.3.4)$, although its region is smaller than that given in Ref. [34] owing to the stability of $[12.6.4]$. Additionally, we have found $[8.6.4; 8^2.4; 12.6.4; 12.8.4]$ to be an unstable tiling pattern at all accessible points in the central region of parameter space considered here.

It is interesting to note that our SCF phase diagram qualitatively agrees well with that computed at $\chi N = 60$ [31] with the exception of $(3.4.6.4)$ and HHL, which were found to be unstable and not considered, respectively; it is possible that $(3.4.6.4)$ was missed in Ref. [31] as it occupies a small region of parameter space, or it may simply become unstable at the stronger segregation. Other than these, it appears that the phase diagrams at $\chi N = 30$ and $\chi N = 60$ are similar, with the stronger segregation primarily causing phase boundaries to shift outwards along the isopleths. For example, along the $f_B = f_C$ isopleth we find HL to be stable for $f_A \in [0.52, 0.60]$; for larger f_A the minority blocks become small enough to allow mixing and thus the formation of L_2. At $\chi N = 60$, however, HL is stable for $f_A \in [0.566, 0.768]$

while L_3 is reduced to a region centered on the $f_A = f_B$ isopleth [31]. Despite this, the phase boundaries of $[6^3]$, $[8^2.4]$, $[8.6.4; 8.6^2]$, and $[10.6.4; 10.6^2]$ remain relatively unchanged, shifting only minorly at $\chi N = 60$ while $[12.6.4]$ replaces HL for $f_A \in [0.513, 0.566]$. In particular, along the $f_B = f_C$ isopleth we find the transition points (i.e., f_A values) between $[8^2.4]/[6^3]$, $[6^3]/[8.6.4; 8.6^2]$, $[8.6.4; 8.6^2]/[10.6.4; 10.6^2]$, and $[10.6.4; 10.6^2]/[12.6.4]$ to lie in-between $[0.28,0.29]$, $[0.39,0.40]$, $[0.44,0.45]$, and $[0.46,0.47]$, respectively, with the corresponding transitions at $\chi N = 60$ given by $f_A = 0.267$, 0.410, 0.457, and 0.513, respectively [31]. This leads to the conclusion that the central region of parameter space is relatively invariant to χN, with the regions of the interior tiling patterns (i.e., $[6^3]$, $[8.6.4; 8.6^2]$, and $[10.6.4; 10.6^2]$) changing little while $[8^2.4]$, $[12.6.4]$, and $(3^2.4.3.4)$ occupy slightly larger regions at $\chi N = 60$ and the region of HL increases significantly.

To support our results in Fig. 3 and better compare with other work, the differences in βf_c among various tiling patterns and lamellar-type phases (i.e., L, HL, HHL, and HTL) along the $f_B = f_C$ isopleth are shown in Fig. 4(a), as well as those in the dimensionless internal energy per star βu_c and the dimensionless entropy per star s_c/k_B in Figs. 4(b) and 4(c), respectively. Along this line the star composition is specified by a single block fraction, f_A, and all the differences in βf_c are taken relative to $[12.6.4]$ rather than the disordered phase so as to highlight their magnitude, which is generally on the order of 10^{-2} for competing phases, except near phase boundaries where it can be on the order of 10^{-3} and rarely 10^{-4} (e.g., at $f_A = 0.6$). There is a general transition from tiling patterns (for $f_A \leqslant 0.5$) to lamellar-type phases ($f_A > 0.5$) along the isopleth, and we note that $[12.6.4]$ is found to be slightly more stable than $[10.6.4; 10.6^2]$ and HL at the two points given by $f_A = 0.48$ and $f_A = 0.50$, respectively.

From Figs. 4(b) and 4(c), we see that βu_c and s_c/k_B of the tiling patterns increase concomitantly with increasing f_A while those of the lamellar-type phases decrease in such a way that they become more stable than the tilings; in other words, the tiling patterns are stabilized (for $f_A \lesssim 0.5$) by βu_c while the lamellar-type phases are stabilized (for $f_A \gtrsim 0.5$) by s_c/k_B. By visually inspecting the morphologies along the isopleth, we find that this effect can be ascribed to the mixing of the minority blocks that occurs in the tiling patterns for larger f_A. This phenomenon is entropically favorable but also incurs energetic penalty, generally large enough to outweigh the entropic gain and result in βf_c larger than the lamellar-type phases for $f_A \gtrsim 0.5$ (which can still maintain three distinct microphase-separated domains at the same f_A). Larger χN would make such mixing more unfavorable and thus favor the tiling patterns as they consistently attain smaller βu_c than the lamellar-type phases. Consequently, since stability at stronger segregations is dominated by energetic effects rather than entropic effects, this explains the larger region occupied by $[12.6.4]$ along the isopleth at $\chi N = 60$ in Ref. [31]. We can see from Fig. 4(b) that $[12.6.4]$ has the smallest βu_c for $f_A \in [0.50, 0.56]$, which nearly overlaps with $f_A \in [0.513, 0.566]$ where $[12.6.4]$ is found to be stable at $\chi N = 60$ [31].

Similar results (data not shown) are found for the case of $f_B > f_C$ (but still within the central portion of the phase
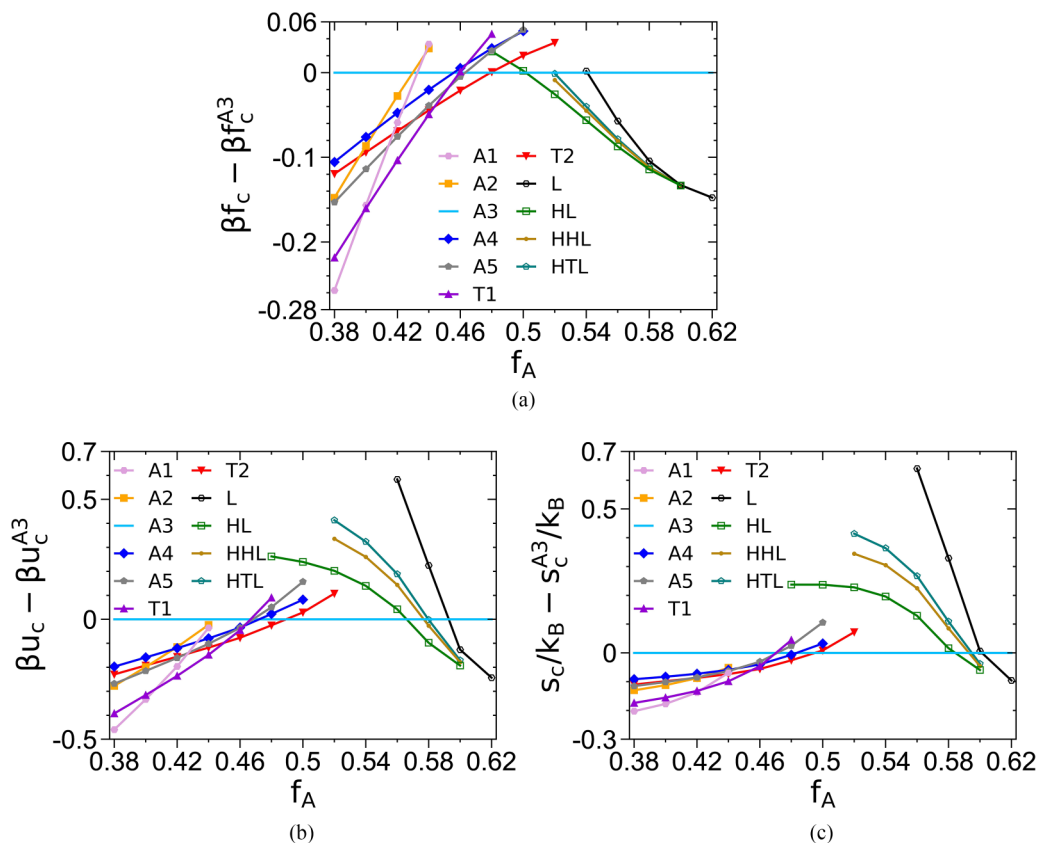
FIG. 4. The dimensionless (a) Helmholtz free energy per star βf_c, (b) internal energy per star βu_c, and (c) entropy per star s_c/k_B along the $f_B = f_C$ isopleth at $\chi N = 30$, for various tiling patterns (including A1 = [6³], A2 = [8².4], A3 = [12.6.4], A4 = (3².4.3.4), A5 = (3.4.6.4), T1 = [8.6.4; 8.6²], and T2 = [10.6.4; 10.6²]) and lamellar-type phases. All values are taken relative to A3. See the main text for more details.

diagram), where [8².4], (3².4.3.4), (3.4.6.4), and [12.6.4] become stable for $f_A \lesssim 0.5$ while HHL becomes stable for $f_A \gtrsim 0.5$.

C. Thermodynamic and morphological properties of complex tiling patterns

Among the tiling patterns formed by ABC stars, (3².4.3.4) and (3.4.6.4) have no direct Archimedean tiling but rather a superimposed one; the unit cells of these stable phases are larger and more complex than other tiling patterns in this system, resulting in an intriguing morphological structure that raises questions concerning the mechanisms behind their stability. Though (3.4.6.4) occupies only a small region of the phase diagram, (3².4.3.4) is quite prominent in this system and is particularly interesting for a number of reasons. It is an example of a cylindrical Frank-Kasper σ phase, having a structure equivalent to the cross section of the spherical σ phase found stable in conformationally asymmetric diblock copolymer melts [46]. It is also closely related (i.e., an approximant) to the DDQC morphology observed experimentally in ABC stars by Matsushita and co-workers [47], which consists of an aperiodic tiling of squares and triangles that cannot be described by a single vertex as (3².4.3.4) can. The existence of such quasicrystalline structures in both soft and hard materials suggests that universal principles govern their behavior, and in ABC stars DDQC forms at compositions close to those of

(3².4.3.4) [19,47]. Finally, theoretical calculations [21] have also shown that (3².4.3.4) could exhibit photonic band gaps if composed of materials of the appropriate dielectric contrast.

In order to understand the stability mechanisms of these unique phases, we calculate the thermodynamic and structural properties described in Sec. IIB for (3².4.3.4), (3.4.6.4), and some competing phases at $\chi N = 30$ and ($f_A = 0.45$, $f_B = 0.30$), where (3².4.3.4) is the stable phase; the results are shown in Fig. 5. The stability of the tiling patterns is governed by relatively subtle differences in their βu_c and s_c/k_B, generally on the order of 10^{-2}. Clearly, (3².4.3.4) is energetically favorable at this point, having the smallest βu_c at the cost of also having the smallest s_c/k_B compared to the competing phases. This trend is observed for nearly every point where (3².4.3.4) is stable, with the exception of ($f_A = 0.43$, $f_B = 0.30$) and ($f_A = 0.43$, $f_B = 0.31$) where [8.6.4; 8.6²] and [8².4], respectively, have the smallest βu_c; (3².4.3.4) is stabilized at these two points by balancing βu_c and s_c/k_B as it also does not have the largest s_c/k_B (data not shown). This is in contrast to the results of Ref. [45] (which considered asymmetrically interacting stars), where (3².4.3.4) was found to exhibit larger s_c/k_B than competing morphologies at a point where it is stable; this could be due to the different interaction parameters. Additionally, although the βf_c of (3².4.3.4) was decomposed into energetic and entropic contributions as a function of f_A at $f_C = 0.2$ and $\chi N = 60$ in Ref. [31], no mechanism behind its stability
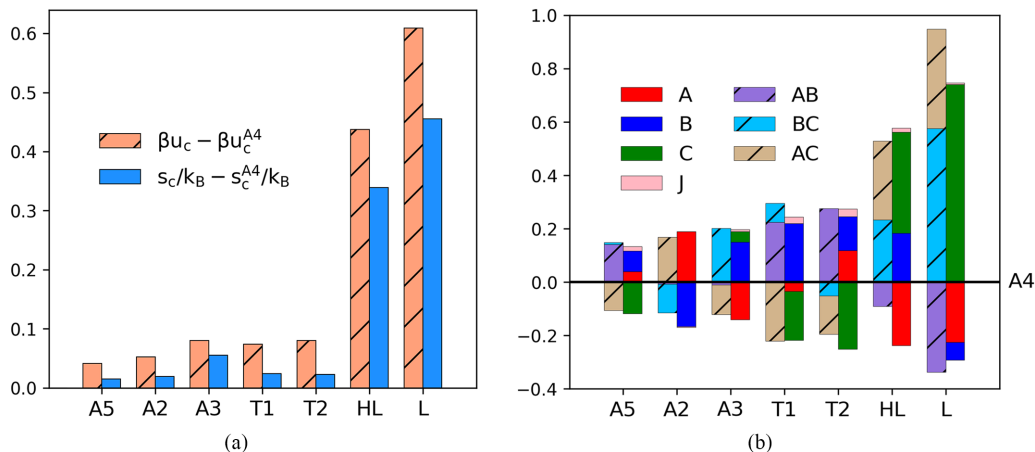
FIG. 5. (a) The dimensionless internal energy per star βu_c and the dimensionless entropy per star s_c/k_B, and (b) various contributions to βu_c (shown as the striped bars) and to s_c/k_B (shown as the solid bars) of A2 = $[8^2.4]$, A3 = $[12.6.4]$, A5 = $(3.4.6.4)$, T1 = $[8.6.4; 8.6^2]$, T2 = $[10.6.4; 10.6^2]$, HL, and L relative to A4 = $(3^2.4.3.4)$ at $\chi N = 30$ and $(f_A = 0.45, f_B = 0.30)$. See the main text for more details.

was noted. The stability mechanism of $(3^2.4.3.4)$ formed by symmetrically interacting stars is therefore elucidated for the first time by our results shown in Figs. 5(a) and 5(b).

$(3.4.6.4)$ has similar properties to $(3^2.4.3.4)$ in Fig. 5(a) as the point $(f_A = 0.45, f_B = 0.30)$ considered there is adjacent to the single point where $(3.4.6.4)$ is stable, i.e., $(f_A = 0.44, f_B = 0.29)$. However, it turns out that neither $(3.4.6.4)$ nor $(3^2.4.3.4)$ has the smallest βu_c at $(f_A = 0.44, f_B = 0.29)$, where $[8.6.4; 8.6^2]$ actually has the smallest βu_c but also prohibitively small s_c/k_B; since $(3.4.6.4)$ has more favorable s_c/k_B, it achieves its stability here by balancing energetic and entropic effects.

Although $(3.4.6.4)$ and $(3^2.4.3.4)$ have similar βu_c and s_c/k_B at $(f_A = 0.45, f_B = 0.30)$ [as shown in Fig. 5(a)], Fig. 5(b) shows that $(3.4.6.4)$ has more favorable AC contribution to βu_c, $\beta u_{c,AC}$, and dimensionless B-block conformational entropy per star, $s_{c,B}/k_B$, while $(3^2.4.3.4)$ has more favorable $\beta u_{c,AB}$ and $s_{c,C}/k_B$. Furthermore, $(3^2.4.3.4)$ exhibits this behavior against most of the competitive tiling patterns (except $[8^2.4]$ and $[12.6.4]$); note that $[8^2.4]$, $[12.6.4]$, and $(3^2.4.3.4)$ have nearly identical $\beta u_{c,AB}$ (thus essentially the same A-B interfacial area) and $s_{c,C}/k_B$, and it is the more favorable $\beta u_{c,AC} + \beta u_{c,BC}$ that stabilizes $(3^2.4.3.4)$ against $[8^2.4]$ and $[12.6.4]$. These results suggest that $(3^2.4.3.4)$ incorporate the thermodynamically favorable features of these two direct Archimedean patterns while simultaneously compensating for their unfavorable energetic properties at the block fractions where $(3^2.4.3.4)$ is stable. As the stable region of $(3^2.4.3.4)$ lies between those of $[8^2.4]$ and $[12.6.4]$ in the phase diagram, this morphology can be considered as a hybridization of the latter two, not only in terms of the thermodynamic properties but also the morphological structure. The square regions of the superimposed Archimedean pattern of $(3^2.4.3.4)$ are identical to a unit cell of $[8^2.4]$ but with larger, distended majority regions while the triangular regions of $(3^2.4.3.4)$ are identical to a unit cell of $[12.6.4]$ but again with distended majority regions. We can therefore conclude that these properties $(\beta u_{c,AB}$ and $s_{c,C}/k_B)$ are some of the defining aspects of $[8^2.4]$, $[12.6.4]$, and $(3^2.4.3.4)$, with the last co-opting such properties from the former two and

augmenting with its own favorable aspects. Other complex tiling patterns could also be considered as hybridizations of the more fundamental patterns, which may allow the design of yet to be discovered morphologies.

Finally, the lamellar-type morphologies (i.e., HL and L) at $(f_A = 0.45, f_B = 0.30)$ have both significantly larger βu_c and s_c/k_B (on the order of 10^{-1}) than the tiling patterns at this point in the parameter space, where it is clear that the energetic cost of forming a lamellar-type morphology is too large for the entropic gain to stabilize it. Both HL and L also exhibit more favorable $\beta u_{c,AB}$ and $s_{c,C}/k_B$ than $(3^2.4.3.4)$, although this is countered by their more unfavorable $\beta u_{c,AC}$ and $\beta u_{c,BC}$. This is particularly apparent for L, which can be attributed to its overlap of the C block with the A and B domains that occurs due to the star architecture, where C microphase-separates as much as possible but must retain a significant amount of contact with B and, to a lesser extent, A. The small $\beta u_{c,AB}$ observed for L results from the screening (or substitution) of interactions between A and B by this layer of C, while simultaneously resulting in its large contact area with A and B. This may be one of the factors that contributes to the destabilization of L at stronger segregations [31].

Another interesting feature of Fig. 5(b) concerns the dimensionless translational entropy per star of the star junctions $s_{c,J}/k_B$, shown for each morphology relative to $(3^2.4.3.4)$. It can be seen that $[8^2.4]$, $[12.6.4]$, and $(3^2.4.3.4)$ have nearly identical $s_{c,J}/k_B$, resulting in their entropic properties being governed solely by the conformational entropy of each block. In contrast, $(3.4.6.4)$, $[8.6.4; 8.6^2]$, and $[10.6.4; 10.6^2]$ exhibit slightly more favorable $s_{c,J}/k_B$ with $[10.6.4; 10.6^2]$ having the largest $s_{c,J}/k_B$ among the phases considered here, although their differences in $s_{c,J}/k_B$ are generally small. This quantity depends solely on the junction density distribution $\rho_J(\mathbf{r})$ of each morphology, given in Fig. 6 for $(3^2.4.3.4)$, $[8^2.4]$, $(3.4.6.4)$, $[8.6.4; 8.6^2]$, and $[10.6.4; 10.6^2]$. Noting that $\rho_J(\mathbf{r})$ represents the probability of finding a star junction at $\mathbf{r}$, we see from Fig. 6 that the junctions are smeared along the domain interfaces rather than tightly aligned along 1D lines (which would be shown as points in the figure), a result attributed
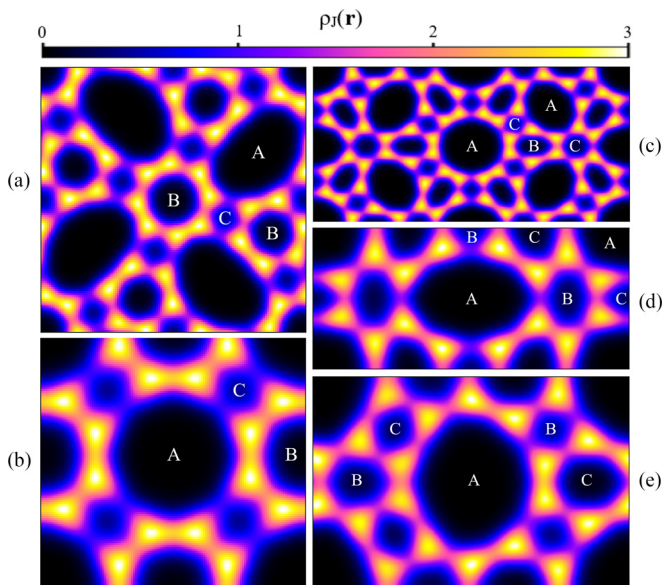
FIG. 6. Junction densities $\rho_J(\mathbf{r})$ for (a) $(3^2.4.3.4)$, (b) $[8^2.4]$, (c) $(3.4.6.4)$, (d) $[8.6.4; 8.6^2]$, and (e) $[10.6.4; 10.6^2]$ at $\chi N = 30$ and $(f_A = 0.45, f_B = 0.30)$, where domains of each species are labeled. Note that all morphologies shown except $[8^2.4]$ have multiple types of domains for some species, in which case one domain of each type is labeled. See the main text for more details.

to the relatively weak segregation at $\chi N = 30$. Despite this smearing, $\rho_J(\mathbf{r})$ still exhibits clear maxima centered on the points where three domains of different species meet.

It is interesting to note that certain domain interfaces appear to be more favorable for the junctions, thus resulting in higher $\rho_J(\mathbf{r})$. This can be seen most clearly for $[8^2.4]$ shown in Fig. 6(b), where $\rho_J(\mathbf{r})$ is the highest at A-B interfaces and the lowest at A-C interfaces. This trend is also found for $(3^2.4.3.4)$ and $(3.4.6.4)$, but not for $[8.6.4; 8.6^2]$ and $[10.6.4; 10.6^2]$ where $\rho_J(\mathbf{r})$ at some A-C interfaces is higher than those at A-B and B-C interfaces. We note that while $[8^2.4]$ has only one type of domains for each species, $(3^2.4.3.4)/[8.6.4; 8.6^2]/[10.6.4; 10.6^2]$ all have two types of B domains, $(3.4.6.4)/[8.6.4; 8.6^2]/[10.6.4; 10.6^2]$ all have two types of C domains, and $(3.4.6.4)/[8.6.4; 8.6^2]$ both have two types of A domains, except that at $(f_A = 0.44, f_B = 0.28)$ along the $f_B = f_C$ isopleth where $[8.6.4; 8.6^2]$ is stable $[8.6.4; 8.6^2]$ has only one type of A domains (but still two types of B and C domains). Apparently, both $[8.6.4; 8.6^2]$ and $[10.6.4; 10.6^2]$ owe their larger $s_{c,J}/k_B$ to their relatively more uniform $\rho_J(\mathbf{r})$ along the interfaces, as shown in Figs. 6(d) and 6(e) by the pink (gray) regions connecting the maxima of $\rho_J(\mathbf{r})$. It is not clear, however, why certain interfaces achieve higher $\rho_J(\mathbf{r})$ than others in the same morphology or why this phenomenon is most pronounced in $[8^2.4]$ compared to other tiling patterns. It appears that the domain area may play a role, with $\rho_J(\mathbf{r})$ at the interfaces between domains of similar areas consistently larger than between domains of large differences in their areas; in other words, $\rho_J(\mathbf{r})$ seems to be larger at the interface with larger "contact" area between domains, but further study is needed to elucidate the cause of this behavior. In all cases, however, we expect that as χN increases, the interfacial area over which the junctions are distributed shrinks significantly for all morphologies, and the junctions eventually approach a 1D alignment in the limit of strong segregation.

IV. CONCLUSIONS

In this work, we have performed numerical polymer SCF calculations of the "standard" model (i.e., incompressible melts of continuous Gaussian chains with the Dirac δ-function interactions) for symmetrically interacting ABC miktoarm triblock terpolymer melts (referred to as stars) using the recently released C++/CUDA version [37] of an open-source software, PSCF [38,39]. The numerical accuracy of our calculations is rigorously tested, and the central region of the phase diagram (in terms of the volume fraction of the P block in the star, f_P with P = A,B,C) constructed at the segregation strength $\chi N = 30$ with a total of 16 candidate phases considered, including one 1D phase, ten 2D phases, and five 3D phases (i.e., those shown in Fig. 1). Eight of these 2D phases are tiling patterns known to form in this system from previous studies [29,31,34], and of these eight tiling patterns we have found seven to be definitively stable at $\chi N = 30$: $[6^3]$, $[8^2.4]$, $[12.6.4]$, $(3^2.4.3.4)$, $(3.4.6.4)$, $[8.6.4; 8.6^2]$, and $[10.6.4; 10.6^2]$. Notably, $(3.4.6.4)$ is reported as stable for the first time, and the 3D phase of HHL is found stable for symmetrically interacting ABC stars for the first time. Our numerical accuracy and careful selection of candidate phases allow the resolution of several outstanding discrepancies from previous SCF studies of the same model system, demonstrating, for example, the stability of $[12.6.4]$, $(3^2.4.3.4)$, and $[10.6.4; 10.6^2]$ and the instability of HTL and $[8.6.4; 8^2.4; 12.6.4; 12.8.4]$, which had conflicting results from previous studies [29,31,34,35]. Finally, we have studied in detail the (mean-field) thermodynamic and morphological properties of two stable complex tiling patterns, $(3^2.4.3.4)$ and $(3.4.6.4)$, and revealed the mechanisms behind their stability. While $(3^2.4.3.4)$ is energetically stabilized in most cases, at a few points the stability of $(3^2.4.3.4)$ and $(3.4.6.4)$ is due to their optimal balance between the energetic and entropic effects. We have also examined the distribution of star junctions in several tiling patterns, and found that certain domain interfaces appear to be more favorable for the junctions; further study is needed to elucidate the cause of this behavior.

Having established the stable and unstable tiling patterns for symmetrically interacting ABC stars at $\chi N = 30$ within the "standard" model using SCF calculations, some logical directions for future work are (1) to systematically increase χN for symmetrically interacting ABC stars, (2) to systematically study the phase behavior of symmetrically interacting ABC stars outside the central region of the f_P parameter space, and (3) to systematically explore the phase behavior of asymmetrically interacting ABC stars. Only two SCF studies [31,35] have been devoted to symmetrically interacting ABC stars at $\chi N = 60$, although it is possible that the center region of the phase diagram (i.e., the region occupied by the tiling patterns) is relatively insensitive to χN as suggested earlier. Most of the existing studies have focused on these tiling patterns as they are unique morphologies that are rarely observed in other polymer systems, and it has been noted [27] that the star architecture's topological constraint is less severe as

the outer regions of the f_P parameter space are approached, resulting in the appearance of familiar morphologies from diblock and linear triblock copolymers. Nevertheless, some theoretical [34,35] and experimental [48] studies on ABC stars have demonstrated the existence of unique 3D morphologies outside of the central region of the f_P parameter space, and it is worthwhile to systematically study the phase behavior of these regions as they are still poorly understood. Finally, only one SCF study [45] has systematically explored the phase behavior of asymmetrically interacting ABC stars (at $\chi_{AB}N = \chi_{BC}N = 30$ and $\chi_{AC}N = 50$). It is our hope that this work will serve as a useful reference for future investigations into the self-assembly of this fascinating class of materials.

ACKNOWLEDGMENT

APPENDIX: RICHARDSON-EXTRAPOLATED PSEUDOSPECTRAL (REPS) METHODS FOR SOLVING THE MODIFIED DIFFUSION EQUATIONS

Here we follow the notation in our main text and take Eq. (4) as an example, which has the formal solution of $q_P(\mathbf{r}, s + ds) = \exp[(\nabla^2 - \omega_P(\mathbf{r}))ds]q_P(\mathbf{r}, s)$. Uniformly discretizing the P-block contour into n_P steps each of

size Δs, the second-order pseudospectral (PS) method [23] gives $q_P(\mathbf{r}, s + \Delta s) \approx \exp(-\omega_P(\mathbf{r})\Delta s/2)\exp(\Delta s\nabla^2)\exp(-\omega_P(\mathbf{r})\Delta s/2)q_P(\mathbf{r}, s)$, which has a *global* error of $O(\Delta s^2)$. Morse and co-workers first pointed out that the error of the PS method contains only even powers of Δs and thus proposed a fourth-order method, which is used in PSCF [38], by linearly extrapolating the two results of $q_P(\mathbf{r}, s + \Delta s)$ obtained via the PS method with the step sizes of Δs and $\Delta s/2$, respectively, to the limit of $\Delta s \to 0$ [40]. This is similar to the (composite) trapezoidal rule for numerical integration, whose error also contains only even powers of the step size; the Kth-order polynomial extrapolation of the $K + 1$ results obtained via the trapezoidal rule with successively halved step sizes to the limit of zero step size then gives the commonly used Romberg integration [49], with $K = 1$ corresponding to the Simpson's 1/3 rule. We therefore refer to the PS method and that proposed by Morse and co-workers [40] as the REPS-0 and REPS-1 methods, respectively, and have implemented the REPS-K (for $K = 0, \ldots, 4$) methods as our improvement to PSCF [43]. Note that the REPS-K method has a global error of $O(\Delta s^{2(K+1)})$; this requires the Romberg integration of the same (or higher) order to calculate the integral in Eq. (2) (e.g., the Simpson's 1/3 rule is used in PSCF to match the REPS-1 method), which in turn requires n_P to be an integer multiple of 2^K [43]; our improved code is freely available at https://github.com/qwcsu/PSCFplus.

[1] F. S. Bates and G. H. Fredrickson, Phys. Today **52**(2), 32 (1999).

[2] C. Park, J. Yoon, and E. L. Thomas, Polymer **44**, 6725 (2003).

[3] F. S. Bates, M. A. Hillmyer, T. P. Lodge, C. M. Bates, K. T. Delaney, and G. H. Fredrickson, Science **336**, 434 (2012).

[4] N. Hadjichristidis, H. Iatrou, M. Pitsikalis, S. Pispas, and A. Avgeropoulos, Prog. Polym. Sci. **30**, 725 (2005).

[5] Y. Matsushita, K. Hayashida, and A. Takano, Macromol. Rapid Commun. **31**, 1579 (2010).

[6] M. Liu, W. Li, F. Qiu, and A.-C. Shi, Macromolecules **45**, 9522 (2012).

[7] L. Li and W. Li, Sci. Sin. Chim. **53**, 651 (2023).

[8] S. Okamoto, H. Hasegawa, T. Hashimoto, T. Fujimoto, H. Zhang, T. Kazama, A. Takano, and Y. Isono, Polymer **38**, 5275 (1997).

[9] S. Sioula, N. Hadjichristidis, and E. L. Thomas, Macromolecules **31**, 8429 (1998).

[10] K. Hayashida, A. Takano, S. Arai, Y. Shinohara, Y. Amemiya, and Y. Matsushita, Macromolecules **39**, 9402 (2006).

[11] Y. Matsushita, K. Hayashida, T. Dotera, and A. Takano, J. Phys.: Condens. Matter **23**, 284111 (2011).

[12] T. Dotera and A. Hatano, J. Chem. Phys. **105**, 8413 (1996).

[13] Y. Bohbot-Raviv and Z. G. Wang, Phys. Rev. Lett. **85**, 3428 (2000).

[14] X. He, L. Huang, H. Liang, and C. Pan, J. Chem. Phys. **116**, 10508 (2002).

[15] X. He, L. Huang, H. Liang, and C. Pan, J. Chem. Phys. **118**, 9861 (2003).

[16] J. G. E. M. Fraaije, J. Chem. Phys. **99**, 9202 (1993).

[17] J. G. E. M. Fraaije, B. A. C. van Vlimmeren, N. M. Maurits, M. Postma, O. A. Evers, C. Hoffmann, P. Altevogt, and G. Goldbeck-Wood, J. Chem. Phys. **106**, 4260 (1997).

[18] T. Gemma, A. Hatano, and T. Dotera, Macromolecules **35**, 3225 (2002).

[19] T. Dotera and T. Gemma, Philos. Mag. **86**, 1085 (2006).

[20] T. Dotera, Philos. Mag. **88**, 2245 (2008).

[21] K. Ueda, T. Dotera, and T. Gemma, Phys. Rev. B **75**, 195122 (2007).

[22] Z. Liu, Z. Wang, Y. Yin, R. Jiang, and B. Li, Soft Matter **17**, 5336 (2021).

[23] Ching-I Huang, H. K. Fang, and C. H. Lin, Phys. Rev. E **77**, 031804 (2008).

[24] Y. Feng, J. Wu, B. Li, and Q. Wang, Soft Matter **18**, 2750 (2022).

[25] Y. Feng, B. Li, and Q. Wang, Soft Matter **18**, 4923 (2022).

[26] F. Drolet and G. H. Fredrickson, Phys. Rev. Lett. **83**, 4317 (1999).

[27] P. Tang, F. Qiu, H. Zhang, and Y. Yang, J. Phys. Chem. B **108**, 8434 (2004).

[28] Z. Guo, G. Zhang, F. Qiu, H. Zhang, Y. Yang, and A. C. Shi, Phys. Rev. Lett. **101**, 028301 (2008).

[29] G. Zhang, F. Qiu, H. Zhang, Y. Yang, and A.-C. Shi, Macromolecules **43**, 2981 (2010).

[30] G. Tzeremes, K. O. Rasmussen, T. Lookman, and A. Saxena, Phys. Rev. E **65**, 041806 (2002).

[31] W. Li, Y. Xu, G. Zhang, F. Qiu, Y. Yang, and A. C. Shi, J. Chem. Phys. **133**, 064904 (2010).

[32] E. W. Cochran, C. J. Garcia-Cervera, and G. H. Fredrickson, Macromolecules **39**, 2449 (2006).

[33] E. W. Cochran, C. J. Garcia-Cervera, and G. H. Fredrickson, Macromolecules **39**, 4264 (2006).

[34] W. Xu, K. Jiang, P. Zhang, and A. C. Shi, J. Phys. Chem. B **117**, 5296 (2013).

[35] M. Qian and Y. Xu, Langmuir **38**, 7889 (2022).

[36] C. A. Tyler and D. C. Morse, Macromolecules **36**, 8184 (2003).

[37] https://github.com/dmorse/pscfpp.

[38] A. Arora, J. Qin, D. C. Morse, K. T. Delaney, G. H. Fredrickson, F. S. Bates, and K. D. Dorfman, Macromolecules **49**, 4675 (2016).

[39] G. K. Cheong, A. Chawla, D. C. Morse, and K. D. Dorfman, Eur. Phys. J. E **43**, 15 (2020).

[40] A. Ranjan, J. Qin, and D. C. Morse, Macromolecules **41**, 942 (2008).

[41] M. W. Matsen, Eur. Phys. J. E **30**, 361 (2009).

[42] A. Arora, D. C. Morse, F. S. Bates, and K. D. Dorfman, J. Chem. Phys. **146**, 244902 (2017).

[43] J. He and Q. Wang, Polymers **16**, 372 (2024).

[44] M. W. Matsen and F. S. Bates, J. Chem. Phys. **106**, 2436 (1997).

[45] K. Jiang, J. Zhang, and Q. Liang, J. Phys. Chem. B **119**, 14551 (2015).

[46] S. Lee, M. J. Bluemle, and F. S. Bates, Science **330**, 349 (2010).

[47] K. Hayashida, T. Dotera, A. Takano, and Y. Matsushita, Phys. Rev. Lett. **98**, 195502 (2007).

[48] J. Park, S. Jang, and J. Kon Kim, J. Polym. Sci., Part B: Polym. Phys. **53**, 1 (2014).

[49] W. H. Press, *Numerical Recipes in C: The Art of Scientific Computing* (Cambridge University Press, Cambridge, New York, 1992).